NANO LETTERS

LETTER

pubs.acs.org/NanoLett

Spontaneous Vortex Nanodomain Arrays at Ferroelectric Heterointerfaces

Christopher T. Nelson,[†] Benjamin Winchester,[‡] Yi Zhang,[†,#] Sung-Joo Kim,[†] Alexander Melville,[§] Carolina Adamo,[§] Chad M. Folkman,[∥] Seung-Hyub Baek,[∥] Chang-Beom Eom,[∥] Darrell G. Schlom,[§] Long-Qing Chen,[‡] and Xiaoqing Pan*[,†]

[†]Department of Materials Science and Engineering, University of Michigan, Ann Arbor, Michigan 48109, United States

[‡]Department of Materials Science and Engineering, Penn State University, University Park, Pennsylvania 16802, United States

[#]National Laboratory of Solid State Microstructures and Department of Materials Science and Engineering, Nanjing University, Nanjing, 210093, P.R. China

[§]Department of Materials Science and Engineering, Cornell University, Ithaca, New York 14853, United States

[∥]Department of Materials Science and Engineering, University of Wisconsin—Madison, Madison,Wisconsin 53706, United States

Supporting Information

ABSTRACT: The polarization of the ferroelectric $BiFeO_3$ subjected to different electrical boundary conditions by heterointerfaces is imaged with atomic resolution using a spherical aberration-corrected transmission electron microscope. Unusual triangular-shaped nanodomains are seen, and their role in providing polarization closure is understood through phase-field simulations. Heterointerfaces are key to the performance of ferroelectric devices, and this first observation of spontaneous vortex nanodomain arrays at ferroelectric heterointerfaces reveals properties unlike the surrounding film including mixed Ising—Néel domain walls, which will affect switching behavior, and a drastic increase of in-plane polarization. The importance of magnetization closure has long been appreciated in multidomain ferromagnetic systems; imaging this analogous effect with atomic resolution at ferroelectric heterointerfaces provides the ability to see device-relevant interface issues. Extension of this technique to visualize domain dynamics is envisioned.

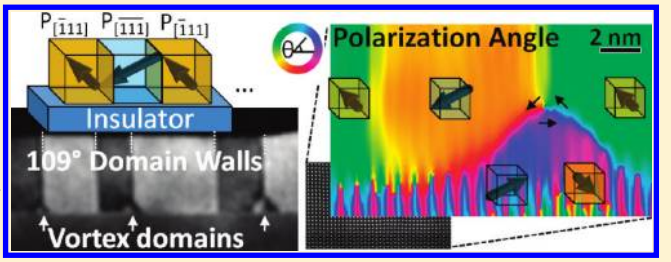

KEYWORDS: Ferroelectricity, multiferroic materials, $BiFeO_3$, transmission electron microscopy, structural characterization

In ferroic materials, the magnetization or polarization may rotate about a point to reduce the magnetic or electric fields. Such vortex domains, well-known to ferromagnetic materials,[1] have only recently been found in ferroelectric nanostructures,[2,3] where they have garnered particular interest for storing memory bits in the vortex state with very little cross-talk between neighboring bits.[4] Polarization vortex structures have also been seen in ferroelectric thin films;[5,6] however they are typically unstable and usually induced by reduced dimensionality. In this work, we report the spontaneous formation of one-dimensional arrays of polarization vortex domains as a result of inhomogeneous electric fields at a heterojunction between a ferroelectric and insulating material.

Strain, crystal defects, and electric charges, all of which can be induced at an interface, strongly affect both the intrinsic properties[7−10] and the domain structure[11−13] of ferroelectric films. Interfaces and defects are known to dominate the kinetics of polarization switching,[14] and domain walls have recently been found to exhibit unique properties such as enhanced conductivity[15] and photocurrent generation.[16] Understanding the critical role that such heterointerfaces, domain walls and defects play requires investigation of the crystal structure and properties at the atomic scale. The recently developed spherical aberration (Cs) correction in transmission electron microscopy (TEM)[17] allows the determination of atomic structure and composition with subangstrom resolution. The ferroelectric polarization can be determined from the atomic displacements measured in atomic resolution TEM images.[15,18,19] Here we use high-resolution TEM (HRTEM) with a point resolution of 0.5 Å in conjunction with computer image processing to obtain atomic-scale quantitative maps of the electric polarization and observe, for the first time, unusual self-assembled, triangular-shaped vortex nanodomains providing polarization closure at ferroelectric heterointerfaces. An analysis of this new type of domain structure reveals properties tremendously different from the surrounding film, including a mixed Ising—Néel character of the domain walls and a drastic increase of in-plane polarization. Although we observe these vortices in a thin film, we show that the depolarization field,

Received: November 30, 2010
Published: January 19, 2011

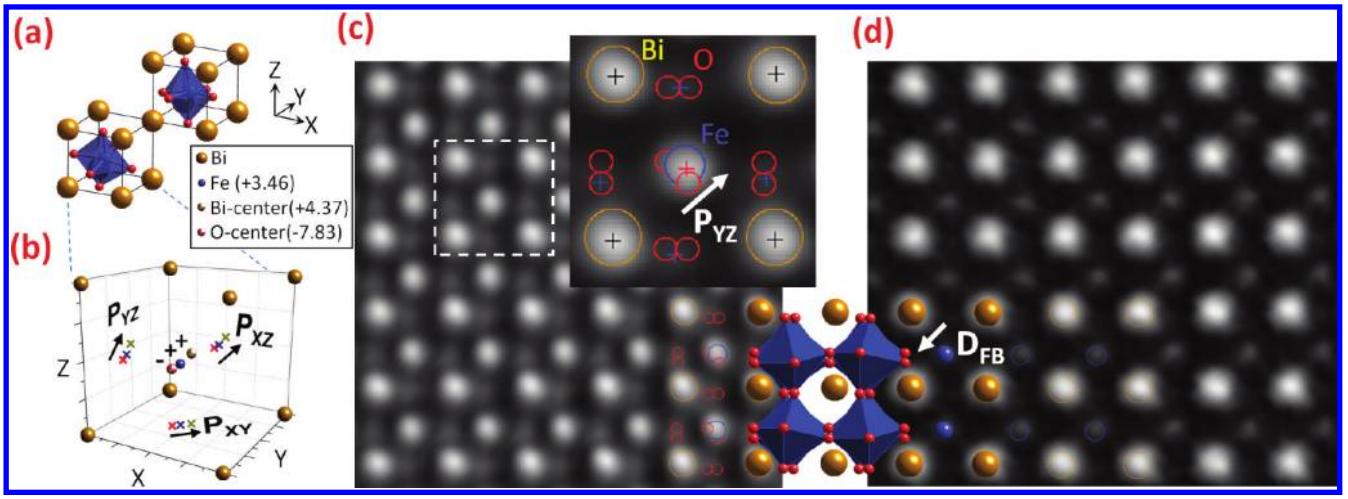

Figure 1. (a) The rhombedral unit cell of bulk $BiFeO_3$ represented as two adjacent pseudocubic perovskite cells. The oxygen octahedra and central Fe cation are clearly displaced from their respective positions at the face and body centers. (b) A polarization along the [111] axis results from the offset of the centers of the positive (Bi and Fe) and negative (O) charges. This offset can be directly observed in the TEM micrograph of a $BiFeO_3$ thin film such as in (c), the phase component of the exit wave determined from a TEM focal series. The atom centers, determined by fit as two-dimensional Gaussians, are shown as crosses in the inset and correspond to a projected polarization of $\mathbf{P_{YZ}} = 82\ \mu C/cm^2$. Since the ion charge centers are all collinear, a much more convenient determination of the polarization direction can be obtained from HAADF-STEM images such as (d) using the relative offsets of the Bi and Fe cations alone ($\mathbf{D_{FB}}$ = 33 pm).

which is the driving force for their formation, is not connected with the reduced dimensionality.

To study the depolarizing effects of the ferroelectric/insulator heterointerface, we choose a model system consisting of $(001)_P$ oriented $BiFeO_3$ thin films on insulating $(110)_O$ $TbScO_3$ single crystal substrates, all grown by molecular-beam epitaxy (MBE) (where the P and O subscripts represent pseudocubic and orthorhombic indices). $BiFeO_3$ is a room temperature multiferroic[20] with a rhombohedral *R*3*c* structure, a large spontaneous polarization ($\sim$100 $\mu C/cm^2$),[21] and correspondingly large physical displacements of the ions, making it suitable for the quantitative analysis of polarization using HRTEM. The $BiFeO_3/TbScO_3$ interface has very little strain due to a small lattice mismatch (<0.14%),[22] which is important for isolating electrical effects since strain can induce instability and rotation of the polarization[23,24] due to a strong electromechanical coupling. To avoid misfit dislocations in the film, we grew $BiFeO_3$ of 20 nm thickness, half the dislocation formation critical thickness determined by the thermodynamic theory.[25]

The structure of $BiFeO_3$ consists of two pseudocubic perovskite unit cells connected along the body diagonal (Figure 1a). The oxygen octahedra and the central Fe cation are displaced along one of the $\langle 111\rangle_P$ directions ($[111]_P$ in Figure 1) from their respective positions at the face and body centers, followed by additional counterrotation of the oxygen octahedra by $\pm 13.8°$ around the $\langle 111\rangle_P$ axes.[26] The polarization can be visualized by assuming valence charges centered on each of the ion sites. For a single pseudocubic unit cell this results in the charge distribution shown in Figure 1b, where the centers of charge for each ion type are shown roughly at the body center of the unit cell. The electric dipole moment along the $[111]_P$ axis is clear from the offset between the negative (O) and positive charges (Fe and Bi). Applying the Born effective charges[27] to this model yields a polarization of 98 $\mu C/cm^2$ along $\langle 111\rangle_P$, in excellent agreement with the measured polarization of $BiFeO_3$.[21,28]

Using HRTEM images, we are able to extract quantitative information about the local polarization vector. Figure 1c shows the phase of the reconstructed electron wave upon exiting a $BiFeO_3$ thin specimen determined from a focus-series of HRTEM images. This approach is one of the few recently developed methods capable of imaging low atomic number, low scattering elements like oxygen in the presence of strongly scattering elements such as bismuth.[29,30] The displacement of the oxygen and iron relative to the center of the bismuth sublattice is clearly visible and the atomic positions match the bulk structure polarized along the $[111]_P$ direction (hollow spheres overlaid on the inset image). If the Born effective charges[27] are assigned to the atom positions in Figure 1c (indicated by crosses) determined using a two-dimensional Gaussian fit, the polarization in the image plane is $|\mathbf{P_{YZ}}| = 82\ \mu C/cm^2$ at an angle of $\Theta = 50°$. This is nearly identical to the value for the bulk structure from Figure 1b projected on the same plane, $|\mathbf{P_{YZ}}| = 80\ \mu C/cm^2$ at $\Theta = 45°$. The increase of the angle from 45° to 50° is consistent with the induced polarization rotation expected in (+0.13%) compressively strained $BiFeO_3$.[24] Assuming an equivalent in-plane polarization normal to the image yields a total polarization of $|\mathbf{P}| = 98\ \mu C/cm^2$, in agreement with the previous model and for the experimental polarization values for $BiFeO_3$ thin films.[21,28]

While the exit wave retrieval approach is useful for determining the anion positions in the $BiFeO_3$ films, because the centers of charge of all three elements are collinear the additional information provided by the oxygen atoms is redundant. Furthermore, the determination of the displacement between the cations alone is more precise; the fit of the cation peak positions in Figure 1c has a 95% confidence interval of ± 0.5 pm compared to ± 2.5 pm for the oxygen peaks. Therefore, we employ simpler and more robust high-angle annular dark field (HAADF) imaging by scanning transmission electron microscopy (STEM) as is shown in Figure 1d. Only the heavier cations are visible in these "*Z*-contrast" images, but they have the advantage that they require no postprocessing and are less sensitive to specimen thickness. We define a vector $\mathbf{D_{FB}}$, which is the atomic displacement in the image plane of the Fe cation from the calculated center of the unit cell formed by its four Bi neighbors. $\mathbf{D_{FB}}$ is determined to be 33 pm along the $[01\bar{1}]_P$ diagonal, which is

dx.doi.org/10.1021/nl1041808 |*Nano Lett.* 2011, 11, 828–834

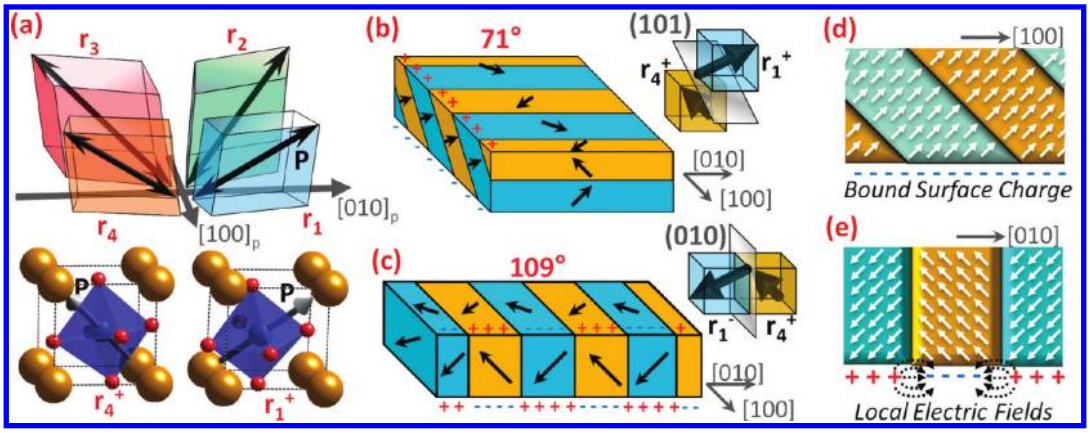

Figure 2. (a) The four ferroelastic variants of the $BiFeO_3$ pseudocubic unit cell, r_1-r_4, with exaggerated elongation of the polarization axis and the corresponding atomic model of upward polarized r_1 and r_4. Twins of these two variants will form domain patterns with 71° rotation of the polarization across $(101)_P$ walls (b) or 109° rotation of the polarization across $(010)_P$ domain walls (c). If uncompensated, these patterns produce the bound surface charges shown in (d) and (e). The surface charge distributions of the 109° pattern produce local electric fields at the surface.

labeled in Figure 1d. The simple relationship between $\mathbf{D}_{FB}$ and the polarization in the image plane is

$$\mathbf{P}_{yz} = -2.5\frac{\mu C}{cm^2 \cdot pm}\cdot \mathbf{D}_{FB} \qquad (1)$$

where $\mathbf{D}_{FB}$ is the displacement in picometers. The linear relationship is straightforward; since $\mathbf{D}_{FB}$ points toward the center of the negative oxygen charges, it is opposite to the polarization direction. By mapping the spatial variation of $\mathbf{D}_{FB}$ in TEM images, using eq 1 we can directly "image" the polarization of $BiFeO_3$.

Polarization of $BiFeO_3$ can be oriented along one of the $\langle 111\rangle_P$ directions resulting in four unique ferroelastic variants r_1-r_4 and eight ferroelectric variants polarized up (+) or down (−) (see Figure 2a where the structural distortion is exaggerated). The small anisotropic strain due to the dissimilar symmetry of $(001)_P$ $BiFeO_3$ and $(110)_O$ $TbScO_3$ leads to the formation of r_1/r_4 ferroelastic twinning structures.[31] In this $(001)_P$ oriented system, this can result in two nonmutually exclusive domain patterns: parallel stripes with an alternating polarization rotating 71° along the in-plane direction separated by inclined $\{011\}_P$ domain walls (Figure 2b) or stripes with a 109° rotation of the polarization separated by vertical $\{010\}_P$ domain walls (Figure 2c).[11] The dominance of one type over the other depends on the minimization of the electrostatic energy.[13] The 71° domain pattern has a smaller polarization rotation but a single out-of-plane polarization vector resulting in a uniform sheet of bound charge on each surface (Figure 2d). If the ferroelectric surfaces are uncompensated by free charges, then the bound charges would produce a large uniform depolarization field. In such an "open circuit" case, the system reduces its electrostatic energy by favoring the alternating out-of-plane polarization of the 109° domain pattern since the net surface charge becomes zero. This reduces the total electrostatic energy and also creates an inhomogeneous depolarization field with large local electric fields at the domain wall terminations where the surface charge changes sign (see Figure 2e).

The local depolarization field occurring at the termination of the vertical 109° domain walls near an uncompensated surface or interface influences the stability of the local polarization orientation and thus domain structure. This effect is clearly demonstrated in the 109° domain pattern of a 20 nm thick $BiFeO_3$ film on $(110)_O$ $TbScO_3$ shown in planar view (Figure 3a) and in cross-sectional (Figure 3b) TEM images. Using the technique described previously, the polarization direction in each domain of the $BiFeO_3$ film can be uniquely indentified since only two polarizations exist in this film, r_1 and r_4, as confirmed by an analysis of the selected area electron diffraction (SAED) patterns of the striped array of domains (See Determination of Ferroelastic Variants and Figure S1 in the Supporting Information). The domain configuration and polarization orientations in Figure 3b, determined by mapping the $\mathbf{D}_{FB}$ vector, are shown schematically below the image.

The strong influence of depolarizing-field effects on the domain pattern can be seen by the addition of an epitaxial $La_{0.7}Sr_{0.3}MnO_3$ bottom electrode (Figure 3c). The free carriers in the $La_{0.7}Sr_{0.3}MnO_3$ buffer screen the bound surface charges at the $BiFeO_3/TbScO_3$ interface, negating the depolarizing field. In this case the $BiFeO_3$ film forms large domains several hundred nanometers in width with little discernible long-range pattern at this length scale separated by domain boundaries typically of paired 109° and 180° domain walls such as the region shown in Figure 3c.

Using subangstrom resolution *Z*-contrast imaging, we imaged the spatial distribution of the $\mathbf{D}_{FB}$ vector in the near surface region of the $BiFeO_3/TbScO_3$ interface to determine the polarization distribution. A *Z*-contrast image of two adjacent 109° domain walls is shown in Figure 4a and the corresponding angle of $\mathbf{D}_{FB}$ in Figure 4b. The pair represents the two types of 109° domain wall terminations at the $BiFeO_3/TbScO_3$ interface: directly terminating (Figure 4a, left) and those forming a triangular pattern of domain walls (Figure 4a, right). The $\mathbf{D}_{FB}$ map shows that the triangle domains consist of a mirrored pair of inclined 180° domain walls, which form a vortex domain structure with the polarization rotating about the intersection of two 109° and two 180° domain walls. The polarization closure is clear in the vector plot of $\mathbf{D}_{FB}$ in Figure 4d (an enlarged region is shown in Figure 3e). No such polarization closure is observed in the $\mathbf{D}_{FB}$ vectors at the direct domain wall termination in Figure 4c (an enlarged region is shown in Figure 3d).

The two triangle domains in the vortex structure exhibit several intriguing properties. First, unlike the narrow domain walls at the film interior, the 180° and 109° domain walls at the vortices have gradual rotations of the polarization vector

dx.doi.org/10.1021/nl1041808 |*Nano Lett.* 2011, 11, 828–834

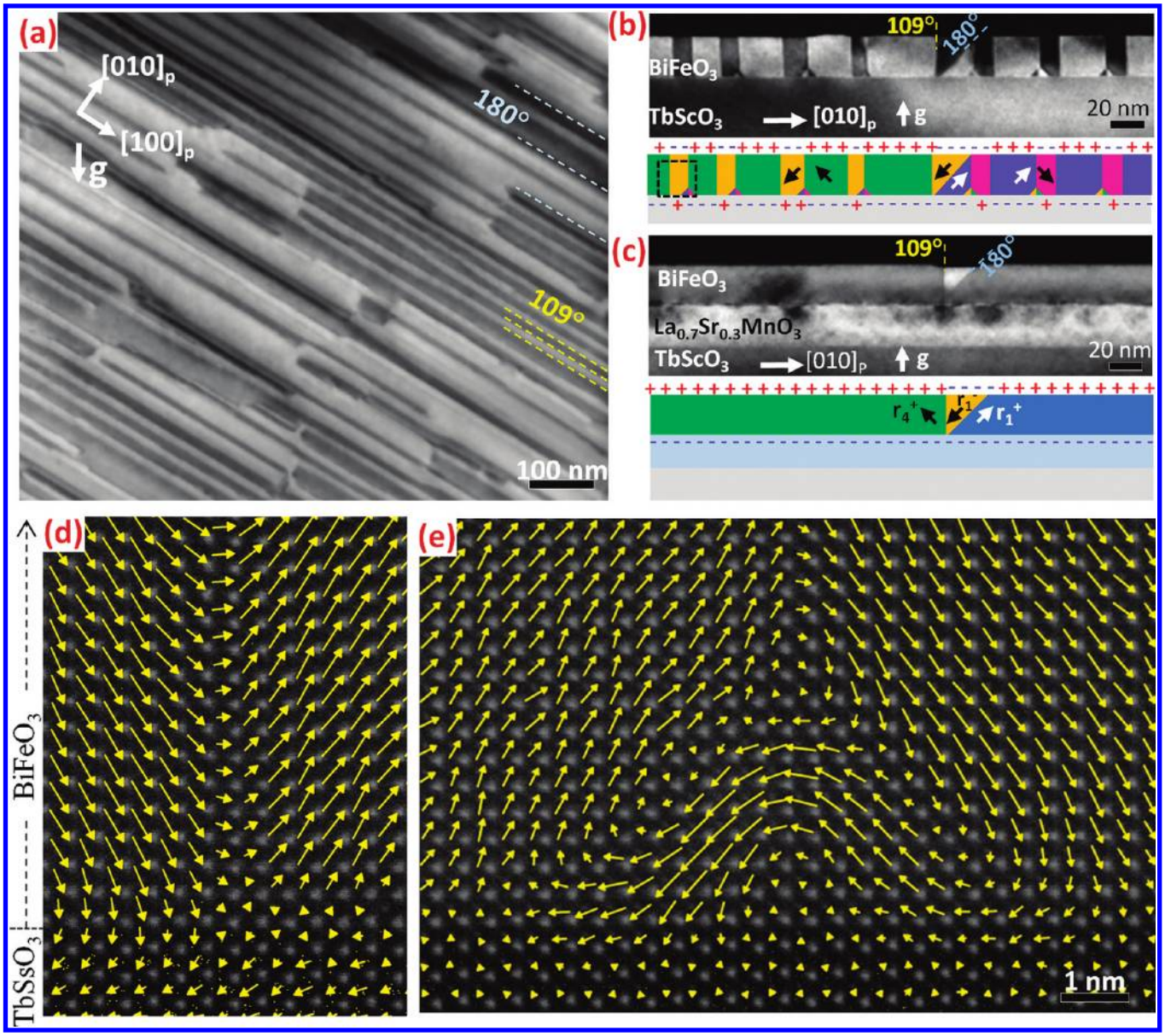

Figure 3. $BiFeO_3$ on insulating $TbScO_3$ forms a $r_1||r_4$ striped domain pattern separated by vertical $(010)_P$ 109° domain walls as seen in planar view (a) and cross sectional (b) dark field TEM. (c) The addition of a conductive 20 nm buffer layer of $La_{0.7}Sr_{0.3}MnO_3$ results in very large domains separated by vertical 109° paired with inclined 180° domain walls. (d) Plot of the iron displacement vectors $\mathbf{D}_{FB}$ for a 109° domain wall which terminates directly with the interface. (e) Plot of the $\mathbf{D}_{FB}$ vectors for a 109° domain wall which forms a vortex domain by addition of a pair of 180° triangle domains.

exhibiting a mixed Néel−Ising character, especially where the 180° domain walls intersect the $TbScO_3$ surface. This leads to the formation of even smaller closure domains at the base of the triangles. The displacement vector extends into the first layer of the substrate suggesting that a polarization may be induced on the $TbScO_3$ surface. Lastly, the in-plane $[010]_P$ component of $\mathbf{D}_{FB}$ within the triangle domains is much larger than its value in the interior of the neighboring domains, as can be seen from both the vector and corresponding magnitude plots (Figure 4d). From a quantitative analysis of $\mathbf{D}_{FB}$ (see Polarization in the near Interface Region and Figure S2 in the Supporting Information), the $[001]_P$ components inside and outside the triangle domains are roughly identical, but the $[010]_P$ components within the triangle 109° domain wall are in some places more than double the value within the interior of the neighboring domains. Since the component along the viewing direction is unknown, a rotation of the polarization along the $[001]_P$ axis cannot be ruled out, but it alone would be insufficient to account for the observed increase. The increased in-plane polarization may be an important factor affecting the local electronic properties of the ferroelectric films since the polarization normal to 109° $BiFeO_3$ domain walls is the driving force for the proposed charge-screening mechanism leading to their conductivity.[15]

The energetic driving force for the formation/stability of the vortex domains is analyzed by comparing the spatial variation of the electrostatic energy and the elastic energy densities for a periodic 109° domain wall array assuming unscreened charges (open-circuit boundary conditions) at the $BiFeO_3$ surfaces (Figure 5a). There is no distinction in elastic energy, but a significant difference in

dx.doi.org/10.1021/nl1041808 |*Nano Lett.* 2011, 11, 828–834

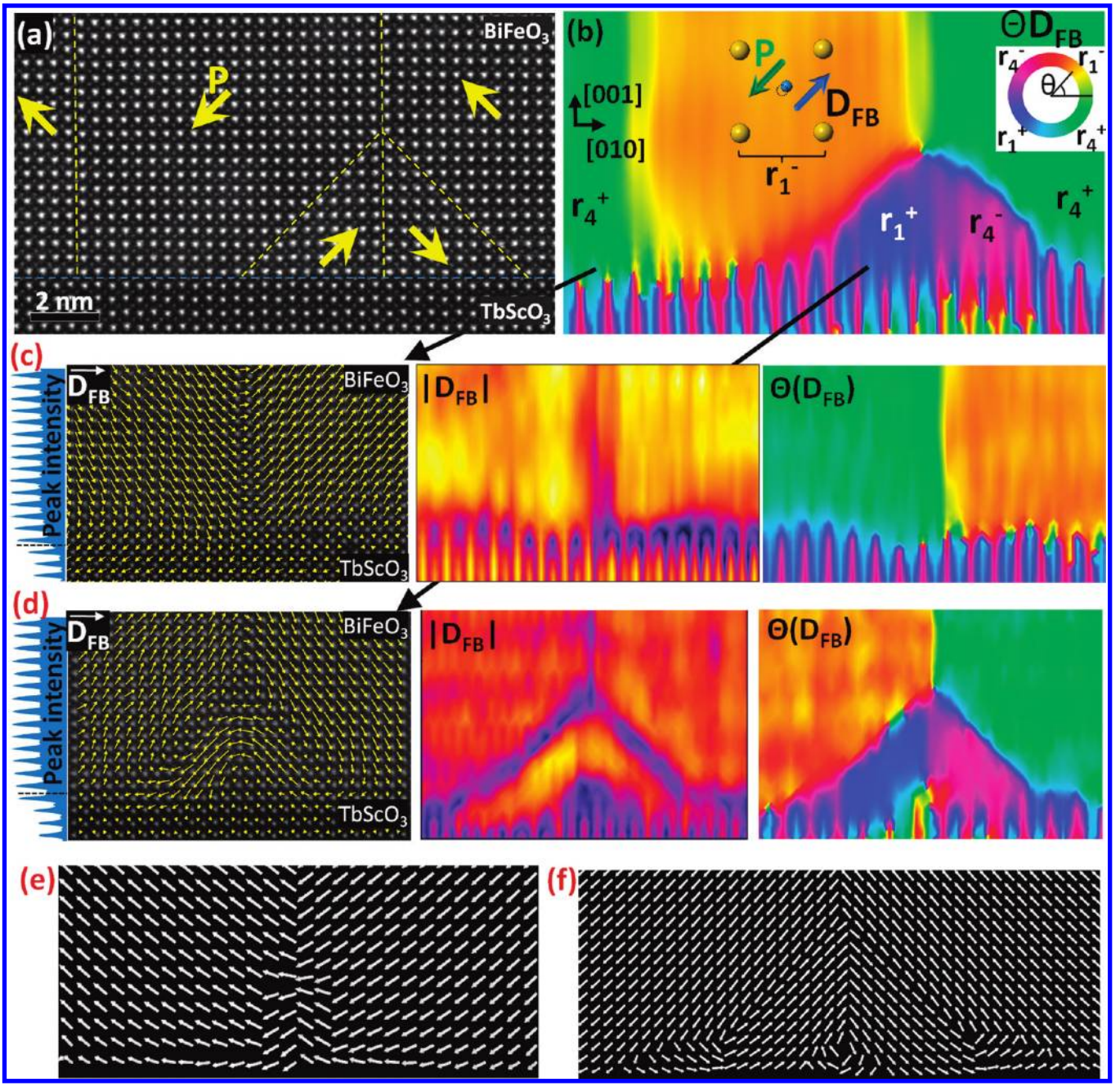

Figure 4. (a) *Z*-contrast STEM image of the intersection of two 109° domain walls with the $TbScO_3$ surface. Yellow arrows indicate polarization direction, and dashed lines indicate the position of the domain walls. (b) A map of the cation displacement $\mathbf{D_{FB}}$ angle corresponding to (a) shows the domain structure of the $BiFeO_3$ and the oscillating Tb position in the substrate. (c) Plot of the vectors for a 109° domain wall which terminates directly with the interface, with corresponding color maps of the magnitude and angle of $\mathbf{D_{FB}}$ shown at right. (d) Plot of the $\mathbf{D_{FB}}$ vectors for a 109° domain wall, which forms a vortex domain, with associated color maps of the magnitude and angle of $\mathbf{D_{FB}}$. The polarization distribution of a directly terminating 109° domain wall (e) and a triangle domain terminating a 109° domain wall (f) from a phase field simulation.

electrostatic energy between the terminations of adjacent 109° domain walls with the substrate. The bound charge distribution (ρ_b) corresponding to this structure (Figure 5b) gives rise to the depolarizing electric field **E**, shown in Figure 5c (black arrows) overlaid with the electrostatic energy. The high electrostatic energy termination (labeled type II) results from the depolarizing field **E** opposing the polarization vector **P**. In contrast, **E** in the low energy domain wall (labeled type I) is more parallel to **P**, corresponding to a relatively small electrostatic energy.

The high energy density of the type II domain wall termination is intrinsically reduced by the insertion of triangular 180° domains, as depicted in Figure 5d. The bound charge of the vortex structure reduces the depolarizing field, and thus the electrostatic energy (Figure 5e), versus the original structure (Figure 5c). This polarization geometry is consistent with the domain patterns and locations observed experimentally (Figure 3b). The local polarization distribution of the type I and vortex-relaxed type II domain wall terminations were

dx.doi.org/10.1021/nl1041808 |*Nano Lett.* 2011, 11, 828–834

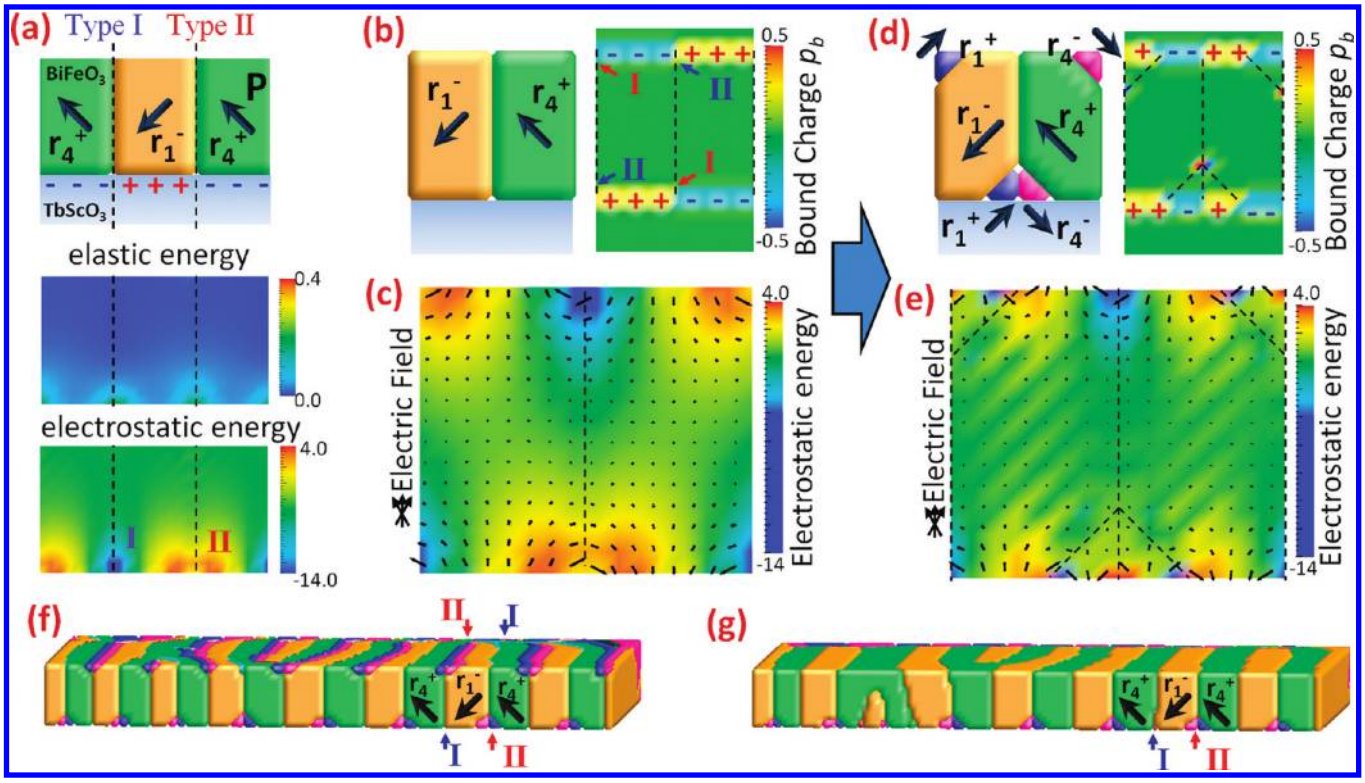

Figure 5. (a) The spatial distribution of the electrostatic and elastic energy density at an insulating surface of an unrelaxed 109° domain structure shows identical elastic energy between adjacent domain walls but distinct low (type I) and high (type II) electrostatic energies. (b) The distribution of the bound charges at the 109° domain wall. (c) A vector plot of the depolarization field overlaid with the electrostatic energy shows it is lowest (type I) when the surface fields are parallel to the in-plane polarization and highest (type II) when opposed. (d) The electrostatic energy is intrinsically decreased by inserting 180° domains to compensate the depolarization field. This inserts a small region with favorably oriented surface charges. (e) The depolarization field, and thus the electrostatic energy, is significantly reduced in the vicinity of the high-energy boundary due to these compensating domains. (f) Phase-field simulation of the $BiFeO_3$ domain structure coalesced from a random r_1/r_4 distribution. The 109° domain pattern formed under open-circuit boundary conditions. (g) The triangle domains disappeared from the top surface after application of short-circuit conditions to that surface.

simulated by the time-dependent Ginzburg−Landau (TDGL) equation[32] (details can be found in the Phase-Field Simulations of the Supporting Information). The resulting polarization distributions at the domain terminations (Figure 4e,f) are in good agreement with the $\mathbf{D}_{FB}$ images (Figure 4c,d).

A simulated domain structure of a $BiFeO_3$ film was obtained by random nucleation of r_1/r_4 domains under open-circuit boundary conditions for both the surface and the film/substrate interface, simulating vacuum growth conditions. The resulting film formed a 109° striped domain pattern with triangle vortex domains at both surfaces (Figure 5f). As illustrated by the $La_{0.7}Sr_{0.3}MnO_3$ buffered film arrangement, the electrostatic energy can also be reduced extrinsically by compensating charges at the interface neutralizing the bound charges. The absence of the vortex domains at the free surface of the $BiFeO_3$ films (Figure 3b) suggests that the depolarizing fields there are not large enough to promote their formation, most likely due to unavoidable screening charges from adsorbed species such as H^+ or OH^- at the top surface.[33] If short-circuit boundary conditions are applied to the top free surface in the simulation representing compensation by such adsorbates generated upon exposure to atmosphere, the triangle domains disappear, and the resulting domain pattern in Figure 5g is a close match to the experimentally observed structure (Figure 3b). That these vortex domains have not been previously observed may likely be due to either strain fields from misfit dislocations or the fact that most typical substrates provide too much charge screening, being either metallic (e.g., having Pt or $SrRuO_3$ bottom electrodes) or semiconducting (e.g., $SrTiO_3$) under typical vacuum growth conditions. Our use of MBE growth, which uses a charge-neutral molecular flux compared to charged plasmas in rf sputtering or pulsed-laser deposition, may also reduce screening.

Since the presence of the vortex domains is dependent only on the local field at the termination of the domain wall, there is no theoretical restriction to low-dimensional systems. We have observed vortex arrays in films up to 800 nm (the thickest we have examined), and they can well be expected to form spontaneously at bulk interfaces. Manipulating the film thickness provides tunability of the array of vortex domains since the 109° domain wall density scales with thickness.[34] Very thin films with two insulating surfaces, for example, would have a large volume fraction of vortex domains. By charge screening one surface, as we have in this experiment, one can produce a film with a single macroscale toroidal moment. Even at large length scales, the vortex domains may significantly alter switching dynamics since reversed domains can grow from existing favorably oriented regions within the vortex domains instead of from a nucleation step.

In summary, we have found a self-assembled array of ferroelectric vortex domains near the interface between a $BiFeO_3$ thin film and an insulating $TbScO_3$ substrate. The driving force for

dx.doi.org/10.1021/nl1041808 |*Nano Lett.* 2011, 11, 828–834

their formation is localized electrostatic energies where 109° domain walls terminate at the interface. The polarization closure is observed by mapping the electric polarization with atomic resolution via HRTEM images and exhibits nonbulk characteristics such as mixed Ising−Néel type domain walls and in-plane polarization up to twice that of the bulk film. Through comparison with phase-field simulations, we infer the presence and absence of free charge carriers at the film/air interface and the film/substrate interface, respectively. Using such an approach, atomic-scale polarization imaging can be applied to study the influence of other defects and interfaces on the properties of ferroelectric materials.

■ ASSOCIATED CONTENT

Supporting Information. Details on film growth, TEM, phase-field simulations, determination of ferroelastic variants via electron diffraction, and details of polarization analysis across vortex domains. This material is available free of charge via the Internet at http://pubs.acs.org.

■ AUTHOR INFORMATION

Corresponding Author
*E-mail: panx@umich.edu.

■ ACKNOWLEDGMENT

This work at the University of Michigan was supported by the Department of Energy (DOE) under Grant DE-FG02-07ER4-6416 and by the National Science Foundation under Grant NSF/DMR-0723032 (TEM instrument). The work at Pennsylvania State University was supported by DOE under Grant DE-FG02-07ER46417. The work at Cornell University was supported by ARO through agreement W911NF-08-2-0032. The work at University of Wisconsin-Madison was supported by ARO under Grant No. W911NF-10-1-0362. The authors also acknowledge the National Center for Electron Microscopy at Lawrence Berkeley National Laboratory for their support under DOE Grant DE-AC02-05CH11231 for user facilities

■ REFERENCES

(1) Kittel, C. *Rev. Mod. Phys.* **1949**, *21* (4), 541–583.
(2) Rodriguez, B. J.; Gao, X. S.; Liu, L. F.; Lee, W.; Naumov, II; Bratkovsky, A. M.; Hesse, D.; Alexe, M. *Nano Lett.* **2009**, *9* (3), 1127–1131.
(3) Schilling, A.; Byrne, D.; Catalan, G.; Webber, K. G.; Genenko, Y. A.; Wu, G. S.; Scott, J. F.; Gregg, J. M. *Nano Lett.* **2009**, *9* (9), 3359–3364.
(4) Naumov, II; Bellaiche, L.; Fu, H. X. *Nature* **2004**, *432* (7018), 737–740.
(5) Ivry, Y.; Chu, D. P.; Scott, J. F.; Durkan, C. *Phys. Rev. Lett.* **2010**, *104* (20), 207602.
(6) Balke, N.; Choudhury, S.; Jesse, S.; Huijben, M.; Chu, Y. H.; Baddorf, A. P.; Chen, L. Q.; Ramesh, R.; Kalinin, S. V. *Nat. Nanotechnol.* **2009**, *4* (12), 868–875.
(7) Choi, K. J.; Biegalski, M.; Li, Y. L.; Sharan, A.; Schubert, J.; Uecker, R.; Reiche, P.; Chen, Y. B.; Pan, X. Q.; Gopalan, V.; Chen, L. Q.; Schlom, D. G.; Eom, C. B. *Science* **2004**, *306* (5698), 1005–1009.
(8) Scott, J. F. *Science* **2007**, *315* (5814), 954–959.
(9) Ramesh, R.; Spaldin, N. A. *Nat. Mater.* **2007**, *6* (1), 21–29.
(10) Haeni, J. H.; Irvin, P.; Chang, W.; Uecker, R.; Reiche, P.; Li, Y. L.; Choudhury, S.; Tian, W.; Hawley, M. E.; Craigo, B.; Tagantsev, A. K.; Pan, X. Q.; Streiffer, S. K.; Chen, L. Q.; Kirchoefer, S. W.; Levy, J.; Schlom, D. G. *Nature* **2004**, *430* (7001), 758–761.
(11) Streiffer, S. K.; Parker, C. B.; Romanov, A. E.; Lefevre, M. J.; Zhao, L.; Speck, J. S.; Pompe, W.; Foster, C. M.; Bai, G. R. *J. Appl. Phys.* **1998**, *83* (5), 2742–2753.
(12) Jang, H. W.; Ortiz, D.; Baek, S. H.; Folkman, C. M.; Das, R. R.; Shafer, P.; Chen, Y.; Nelson, C. T.; Pan, X.; Ramesh, R.; Eom, C. B. *Adv. Mater.* **2009**, *21* (7), 817–823.
(13) Chu, Y. H.; He, Q.; Yang, C. H.; Yu, P.; Martin, L. W.; Shafer, P.; Ramesh, R. *Nano Lett.* **2009**, *9* (4), 1726–1730.
(14) Jesse, S.; Rodriguez, B. J.; Choudhury, S.; Baddorf, A. P.; Vrejoiu, I.; Hesse, D.; Alexe, M.; Eliseev, E. A.; Morozovska, A. N.; Zhang, J.; Chen, L. Q.; Kalinin, S. V. *Nat. Mater.* **2008**, *7* (3), 209–215.
(15) Seidel, J.; Martin, L. W.; He, Q.; Zhan, Q.; Chu, Y. H.; Rother, A.; Hawkridge, M. E.; Maksymovych, P.; Yu, P.; Gajek, M.; Balke, N.; Kalinin, S. V.; Gemming, S.; Wang, F.; Catalan, G.; Scott, J. F.; Spaldin, N. A.; Orenstein, J.; Ramesh, R. *Nat. Mater.* **2009**, *8* (3), 229–234.
(16) Yang, S. Y.; Seidel, J.; Byrnes, S. J.; Shafer, P.; Yang, C. H.; Rossell, M. D.; Yu, P.; Chu, Y. H.; Scott, J. F.; Ager, J. W.; Martin, L. W.; Ramesh, R. *Nat. Nanotechnol.* **2010**, *5* (2), 143–147.
(17) Urban, K. W. *Science* **2008**, *321* (5888), 506.
(18) Jia, C. L.; Nagarajan, V.; He, J. Q.; Houben, L.; Zhao, T.; Ramesh, R.; Urban, K.; Waser, R. *Nat. Mater.* **2007**, *6* (1), 64–69.
(19) Jia, C. L.; Mi, S. B.; Urban, K.; Vrejoiu, I.; Alexe, M.; Hesse, D. *Nat. Mater.* **2008**, *7* (1), 57–61.
(20) Wang, J.; Neaton, J. B.; Zheng, H.; Nagarajan, V.; Ogale, S. B.; Liu, B.; Viehland, D.; Vaithyanathan, V.; Schlom, D. G.; Waghmare, U. V.; Spaldin, N. A.; Rabe, K. M.; Wuttig, M.; Ramesh, R. *Science* **2003**, *299* (5613), 1719–1722.
(21) Das, R. R.; Kim, D. M.; Baek, S. H.; Eom, C. B.; Zavaliche, F.; Yang, S. Y.; Ramesh, R.; Chen, Y. B.; Pan, X. Q.; Ke, X.; Rzchowski, M. S.; Streiffer, S. K. *Appl. Phys. Lett.* **2006**, *88* (24), No. 242904.
(22) Velickov, B.; Kahlenberg, V.; Bertram, R.; Uecker, R. *Acta Crystallogr., Sect. E: Struct. Rep. Online* **2008**, *64*, I79–U64.
(23) Chu, M. W.; Szafraniak, I.; Scholz, R.; Harnagea, C.; Hesse, D.; Alexe, M.; Gosele, U. *Nat. Mater.* **2004**, *3* (2), 87–90.
(24) Jang, H. W.; Baek, S. H.; Ortiz, D.; Folkman, C. M.; Das, R. R.; Chu, Y. H.; Shafer, P.; Zhang, J. X.; Choudhury, S.; Vaithyanathan, V.; Chen, Y. B.; Felker, D. A.; Biegalski, M. D.; Rzchowski, M. S.; Pan, X. Q.; Schlom, D. G.; Chen, L. Q.; Ramesh, R.; Eom, C. B. *Phys. Rev. Lett.* **2008**, *101* (10), No. 107602.
(25) Matthews, J. W.; Blakeslee, A. E. *J. Cryst. Growth* **1974**, *27* (DEC), 118–125.
(26) Kubel, F.; Schmid, H. *Acta Crystallogr., Sect. B: Struct. Sci.* **1990**, *46*, 698–702.
(27) Neaton, J. B.; Ederer, C.; Waghmare, U. V.; Spaldin, N. A.; Rabe, K. M. *Phys. Rev. B* **2005**, *71* (1), No. 014113.
(28) Li, J. F.; Wang, J. L.; Wuttig, M.; Ramesh, R.; Wang, N.; Ruette, B.; Pyatakov, A. P.; Zvezdin, A. K.; Viehland, D. *Appl. Phys. Lett.* **2004**, *84* (25), 5261–5263.
(29) Kisielowski, C.; Hetherington, C. J. D.; Wang, Y. C.; Kilaas, R.; O'Keefe, M. A.; Thust, A. *Ultramicroscopy* **2001**, *89* (4), 243–263.
(30) Jia, C. L.; Lentzen, M.; Urban, K. *Science* **2003**, *299* (5608), 870–873.
(31) Folkman, C. M.; Baek, S. H.; Jang, H. W.; Eom, C. B.; Nelson, C. T.; Pan, X. Q.; Li, Y. L.; Chen, L. Q.; Kumar, A.; Gopalan, V.; Streiffer, S. K. *Appl. Phys. Lett.* **2009**, *94* (25), No. 251911.
(32) Chen, L. Q. *J. Am. Ceram. Soc.* **2008**, *91* (6), 1835–1844.
(33) Fong, D. D.; Kolpak, A. M.; Eastman, J. A.; Streiffer, S. K.; Fuoss, P. H.; Stephenson, G. B.; Thompson, C.; Kim, D. M.; Choi, K. J.; Eom, C. B.; Grinberg, I.; Rappe, A. M. *Phys. Rev. Lett.* **2006**, *96* (12), No. 127601.
(34) Huang, C. W.; Chen, L.; Wang, J.; He, Q.; Yang, S. Y.; Chu, Y. H.; Ramesh, R. *Phys. Rev. B* **2009**, *80* (14), No. 140101.